

# Additive-Free $\text{Nb}_2\text{O}_5$ – $\text{TiO}_2$ Hybrid Anode towards Low-Cost and Safe Lithium-Ion Batteries: A Green Electrode Material Produced in an Environmentally Friendly Process

Md Mokhlesur Rahman,\*<sup>[a]</sup> Mengqi Zhou,<sup>[a]</sup> Irin Sultana,<sup>[a]</sup> Srikanth Mateti,<sup>[a]</sup> Alexey Falin,<sup>[a]</sup> Lu Hua. Li,<sup>[a]</sup> Zhong-Shuai Wu,<sup>[b]</sup> and Ying Chen\*<sup>[a]</sup>

The development of additive-free electrodes based on low-cost and environmentally friendly materials is one of the major challenges for expanding sustainable and ecologically friendly energy storage. Most conventional electrode preparation processes are currently facing a problem: the addition of various additives/chemicals, particularly binder, carbon black and toxic *N*-Methyl-2-pyrrolidone. These additives increase the production cost, decrease the energy and power density of the battery and are environmental hazards. Herein, a  $\text{Nb}_2\text{O}_5$ – $\text{TiO}_2$  hybrid electrode for lithium-ion batteries is fabricated by adopting the advanced radio frequency sputtering technique, which requires no supplementary support from additives/chemicals. The

$\text{Nb}_2\text{O}_5$ – $\text{TiO}_2$  electrode reveals high capacity (gravimetric: 214 mAh g<sup>-1</sup> at 50 mA g<sup>-1</sup>; areal: 0.0214 mAh cm<sup>-2</sup> at 5  $\mu\text{A}$  cm<sup>-2</sup>; volumetric: 1,813 mAh cm<sup>-3</sup> at 5  $\mu\text{A}$  cm<sup>-2</sup>), long-term cyclic stability (gravimetric: 174 mAh g<sup>-1</sup> at 0.4 A g<sup>-1</sup>; areal: 0.0174 mAh cm<sup>-2</sup> at 40  $\mu\text{A}$  cm<sup>-2</sup>; volumetric: 1,474 mAh cm<sup>-3</sup> at 40  $\mu\text{A}$  cm<sup>-2</sup> after 1000 cycles) and superior rate capability (gravimetric: 115 mAh g<sup>-1</sup> at 6.0 A g<sup>-1</sup>; areal: 0.0115 mAh cm<sup>-2</sup> at 6 mA cm<sup>-2</sup>; volumetric: 974 mAh cm<sup>-3</sup> at 6 mA cm<sup>-2</sup>), which are better than other reported systems. Such a green chemistry strategy of fabricating additive-free electrodes opens up new ways for the development of sustainable and robust energy storage technologies.

## 1. Introduction

Lithium-ion batteries (LIBs) are considered as the leading candidates for hybrid, plug-in hybrid, and all electrical vehicles, and possibly for utility applications as well. Considering the progress in large-scale applications, the next generation of LIBs is selected on the basis of their safety/environmental friendliness, cost and energy capacity, which largely depends on the electrode materials used.<sup>[1–3]</sup> Currently, commercial anodes are made of graphite that still suffers from potential safety issues (thermal runaway), with the formation of lithium dendrites and a solid-electrolyte interphase (SEI) layer, owing to its low lithiation potential (0.2 V vs Li/Li<sup>+</sup>), especially when the LIBs are operated at high current rates.<sup>[4–7]</sup> Therefore, to address all of these issues, an alternative anode needs to be developed. Being inherently safe and chemically compatible with the electrolyte, low voltage insertion for Li<sup>+</sup> and fast Li<sup>+</sup> insertion/removal host as well as low environmental impact and cost,<sup>[8,9]</sup> titanium-oxide-based materials, including both Li-titanates and

various  $\text{TiO}_2$  polymorphs, are considered to be alternatives to carbonaceous anodes in LIBs. The rutile phase of  $\text{TiO}_2$  is the most common natural form, as it is the most thermodynamically stable phase under standard conditions and capable to provide high capacity and better lithium electrochemical activity in its nanostructured form.<sup>[10,11]</sup> However, nanostructured  $\text{TiO}_2$  is prone to suffer from severe aggregation, which dramatically diminishes its rate capability and cyclability.<sup>[12]</sup>

In addition to rutile  $\text{TiO}_2$ , niobium pentoxide ( $\text{Nb}_2\text{O}_5$ ) is also an ideal high power electrode material in LIBs, as it is relatively inexpensive, environmentally benign, stable in a wide range of temperature and pH conditions, and most importantly improved cell safety due to a higher discharge cut-off voltage ( $\geq 1.0$  V vs Li/Li<sup>+</sup>) which reduces dangerous high-temperature reactions.<sup>[13–16]</sup> However, its intrinsic poor electronic conductivity and capacity decay resulted from pulverization during charge-discharge process limit its practical application in LIBs. Also, it is still challenging to develop efficient but simple ways to enhance the utilization of electroactive  $\text{Nb}_2\text{O}_5$ .<sup>[13,17–20]</sup>

To circumvent these problems with  $\text{TiO}_2$  and  $\text{Nb}_2\text{O}_5$ , the hybridization concept can potentially be used. It has been demonstrated that hybrid oxide systems exhibit some new properties and superior to single-phase oxides, the hybrid systems integrate several types of functional materials that can synergistically enhance the intrinsic properties of each component such as electrical/ionic conductivity, electrochemical reactivity, and mechanical stability.<sup>[21–25]</sup> The underlying problem with the conventional procedure for the preparation of battery electrodes is time consuming involving unhealthy multiple steps, including materials synthesis with toxic reagents, slurry formation, coating onto current collectors, and drying in

[a] Dr. M. Mokhlesur Rahman, Dr. M. Zhou, Dr. I. Sultana, Dr. S. Mateti, Dr. A. Falin, Dr. L. H. Li, Prof. Y. Chen  
Institute for Frontier Materials  
Deakin University  
Geelong Waurn Ponds, VIC 3216 (Australia)  
E-mail: m.rahman@deakin.edu.au  
ian.chen@deakin.edu.au

[b] Prof. Z.-S. Wu  
Dalian National Laboratory for Clean Energy  
Dalian Institute of Chemical Physics  
Chinese Academy of Sciences  
457 Zhongshan Road, Dalian 116023 (China).

 Supporting information for this article is available on the WWW under <https://doi.org/10.1002/batt.201800092>

vacuum. Furthermore, carbon black, polymeric binders and organic solvent (*N*-Methyl-2-pyrrolidone) are commonly included during slurry preparation for electrical conduction and better physical contacts between particles and current collector, respectively.<sup>[26–30]</sup> Basically, addition of various additives to the electrodes generates 3 major problems:<sup>[31,32]</sup> i) an extra weight (10–40%, depending on the electrode materials used) of the electrode is increased; ii) inhomogeneous blend of carbon black, binders, and nanoparticles (active materials) makes the diffusion paths of the ions and electrons unclear, leading to model and characterization difficulties; and iii) complicated procedure and various additives lead to environmental hazard as well as high cost of the electrodes.

Previously, nanomaterials in the form of nanowires and nanotubes with no binder and carbon have been developed and investigated as electrodes for energy storage.<sup>[33–37]</sup> However, fully additive-free electrode films in the form of nanoparticles are hardly reported. More specifically, the hybridization of both nanoparticles of  $\text{TiO}_2$  and  $\text{Nb}_2\text{O}_5$  as an additive-free electrode has not yet been established. In 2016, hybridization of Nb-doped  $\text{TiO}_2$  and  $\text{Nb}_2\text{O}_5$  was studied by Yu et al.<sup>[38]</sup> In that study, they fabricated core-shell heterostructures where Nb-doped  $\text{TiO}_2$  rod used as a core and  $\text{Nb}_2\text{O}_5$  nanosheet as a shell. Recently, Liu et al.<sup>[12]</sup> have also demonstrated a heterogeneous composite of  $\text{TiO}_2$ – $\text{Nb}_2\text{O}_5$ . In this composite, nanoparticles of  $\text{TiO}_2$  were surrounded on the nanosheets of  $\text{Nb}_2\text{O}_5$ . However, the above-mentioned hybridized systems cannot be claimed as additive-free systems as they used binder and carbon black for the preparation of electrode. Moreover, various reagents were used in their synthesis process. Despite the tremendous research efforts devoted to investigating a wide variety of hybrid materials for electrochemical performances in recent years, however, the hybrid systems are still limited to high crystalline ones incorporated with high level of binder and carbon additives.<sup>[39–41]</sup> Hence, it would be advantageous but quite challenging to develop a simplistic method of fabrication binary electrode system, particularly metal oxide without using any additives/chemicals but with superior electrochemical performances.

Herein, we for the first time report additive free  $\text{Nb}_2\text{O}_5$ – $\text{TiO}_2$  electrode deposited on Cu foil fabricated by hybridization of both nanoparticles of  $\text{TiO}_2$  and  $\text{Nb}_2\text{O}_5$  via ultrafast sputtering technique by combining titanium (Ti) and niobium (Nb) target together at the same time. Most importantly, no reagents were used in this synthesis process. The obtained hybridized  $\text{Nb}_2\text{O}_5$ – $\text{TiO}_2$  electrode was used directly without further incorporation of any carbon, binder or organic solvent. A single oxide electrode of  $\text{Nb}_2\text{O}_5$  and  $\text{TiO}_2$  was also fabricated for comparison, using same technique. A series of electrodes with different deposition times of 0.5, 1.0, and 2.0 h was fabricated and electrodes were identified as  $\text{Nb}_2\text{O}_5$ – $\text{TiO}_2$  (0.5 h),  $\text{Nb}_2\text{O}_5$ – $\text{TiO}_2$  (1 h),  $\text{Nb}_2\text{O}_5$ – $\text{TiO}_2$  (2 h),  $\text{Nb}_2\text{O}_5$  (1 h), and  $\text{TiO}_2$  (1 h), respectively. The electrode was operated within the safe potential window of 1.0–3.0 V (vs Li/ $\text{Li}^+$ ) and hybrid  $\text{Nb}_2\text{O}_5$ – $\text{TiO}_2$  (1 h) electrode with special pearls-chain like morphology delivers a promising reversible capacity of gravimetric 214  $\text{mAh g}^{-1}$  at 50  $\mu\text{A cm}^{-2}$ ; areal 0.0214  $\text{mAh cm}^{-2}$  at 5  $\mu\text{A cm}^{-2}$

and volumetric 1,813  $\text{mAh cm}^{-3}$  at 5  $\mu\text{A cm}^{-2}$  after 500 cycles. The electrode exhibits superior long-term cyclic stability with a retained capacity of gravimetric 174  $\text{mAh g}^{-1}$  at 0.4  $\text{A g}^{-1}$ ; areal 0.0174  $\text{mAh cm}^{-2}$  at 40  $\mu\text{A cm}^{-2}$  and volumetric 1,474  $\text{mAh cm}^{-3}$  at 40  $\mu\text{A cm}^{-2}$  even after 1000 cycles. The rate capability of the  $\text{Nb}_2\text{O}_5$ – $\text{TiO}_2$  (1 h) is quite high and a reversible capacity of gravimetric 115  $\text{mAh g}^{-1}$  at 6.0  $\text{A g}^{-1}$ ; areal 0.0115  $\text{mAh cm}^{-2}$  at 6  $\text{mA cm}^{-2}$  and volumetric 974  $\text{mAh cm}^{-3}$  at 6  $\text{mA cm}^{-2}$  is achieved. These results demonstrate that additive-free  $\text{Nb}_2\text{O}_5$ – $\text{TiO}_2$  materials have great potential to be used as safe electrode for LIBs. Moreover, such a special electrode architecture can be used in Li-ion micro-batteries, as it demands high energy and high power on a small footprint area.

## 2. Results and Discussion

Figure 1a compares the XRD patterns of the hybrid  $\text{Nb}_2\text{O}_5$ – $\text{TiO}_2$  (0.5 h),  $\text{Nb}_2\text{O}_5$ – $\text{TiO}_2$  (1 h), and  $\text{Nb}_2\text{O}_5$ – $\text{TiO}_2$  (2 h) electrodes. All

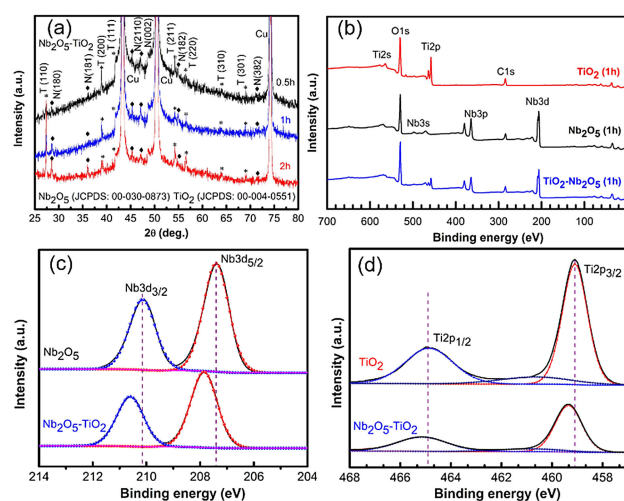


**Figure 1.** a) XRD patterns of the  $\text{Nb}_2\text{O}_5$ – $\text{TiO}_2$  (0.5 h),  $\text{Nb}_2\text{O}_5$ – $\text{TiO}_2$  (1 h), and  $\text{Nb}_2\text{O}_5$ – $\text{TiO}_2$  (2 h) electrodes. b) wide survey scan of XPS of the  $\text{Nb}_2\text{O}_5$ – $\text{TiO}_2$  (1 h)  $\text{Nb}_2\text{O}_5$  (1 h) and  $\text{TiO}_2$  (1 h) electrodes. c) high-resolution XPS spectra of Nb3d region. d) high-resolution XPS spectra of Ti2p region.

XRD patterns consist of mixed metal oxide phases of  $\text{Nb}_2\text{O}_5$  and  $\text{TiO}_2$ , respectively. Diffraction peaks for the  $\text{Nb}_2\text{O}_5$  are indexed to the orthorhombic crystal structure (JCPDS Card No. 00-030-0873) and peaks are located at around 28.5, 36.7, 45.0, 46.1, 55.0, and 71.2°, which are assigned to the (180), (181), (2110), (002), (182), and (382) reflections, respectively. In the case of  $\text{TiO}_2$ , all diffraction peaks are well indexed to the rutile  $\text{TiO}_2$  phase (JCPDS Card No. 00-004-0551) with tetragonal crystal system. The diffraction peaks for rutile  $\text{TiO}_2$  are located at 27.4, 39.1, 41.2, 54.3, 56.6, 64.0, and 68.9°, corresponding to the (110), (200), (111), (211), (220), (310), and (301) reflections, respectively. It is visualised that  $\text{Nb}_2\text{O}_5$ – $\text{TiO}_2$  (2 h) electrode shows strong diffraction peaks, which may be due to longer deposition time. No other peaks for anatase or brookite were detected in the electrode, signifying  $\text{Nb}_2\text{O}_5$ – $\text{TiO}_2$  electrode

composes of only rutile  $\text{TiO}_2$  and orthorhombic  $\text{Nb}_2\text{O}_5$ . To further confirm the composition of  $\text{Nb}_2\text{O}_5-\text{TiO}_2$  electrode, X-ray photoelectron spectroscopy (XPS) was carried out (Figure 1b-d). Species of Nb, Ti, O, and C are detected as elements in the  $\text{Nb}_2\text{O}_5-\text{TiO}_2$  electrode, suggesting high purity of the sample (Figure 1b). High-resolution XPS spectra for the Nb3d region shows two peaks at around 207.9 eV for  $\text{Nb}3\text{d}_{5/2}$  and 210.5 eV for  $\text{Nb}3\text{d}_{3/2}$  regions (Figure 1c), in good agreement with the binding energies of  $\text{Nb}_2\text{O}_5$ <sup>[16,42]</sup> confirming the presence of  $\text{Nb}_2\text{O}_5$  in the  $\text{Nb}_2\text{O}_5-\text{TiO}_2$  electrode. Similarly, two peaks of Ti2p are centred at 459 and 465 eV for the regions of  $\text{Ti}2\text{p}3/2$  and  $\text{Ti}2\text{p}1/2$ , respectively (Figure 1d), indicative of the existence of  $\text{TiO}_2$  in the hybrid electrode.<sup>[43,44]</sup>

Surface morphologies of the  $\text{Nb}_2\text{O}_5-\text{TiO}_2$  electrode films as a function of deposition time were analysed by SEM (Figure 2). It is clearly seen that surface morphologies of the electrode films feature pearls-chain like structure composed of nano-

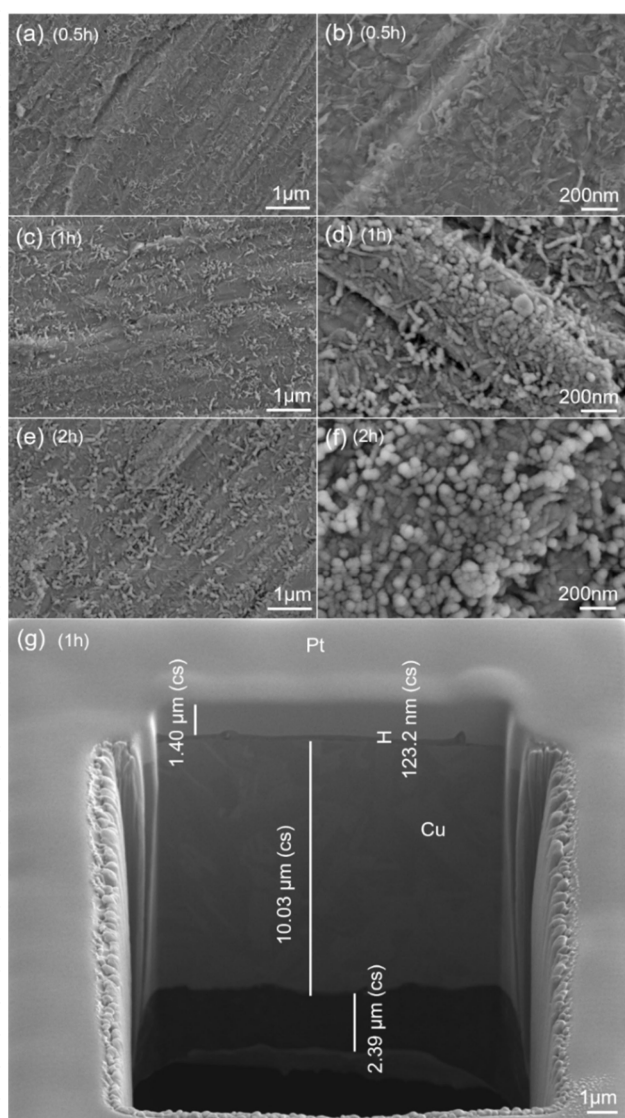


**Figure 2.** SEM images of the electrodes: a, b)  $\text{Nb}_2\text{O}_5-\text{TiO}_2$  (0.5 h). c, d)  $\text{Nb}_2\text{O}_5-\text{TiO}_2$  (1 h). e, f)  $\text{Nb}_2\text{O}_5-\text{TiO}_2$  (2 h); and g) cross-section image of the  $\text{Nb}_2\text{O}_5-\text{TiO}_2$  (1 h) electrode.

particles. The formation of pearls-chain is not obvious when the deposition time is shorter (0.5 h) (Figure 2a, b) and longer (2 h) (Figure 2e, f) as well. The formation of pearls-chain became more significant with the deposition time of 1 h (Figure 2 c, d). The films deposited over 2 h, however, exhibits much coarser particles than that of 1 h and 0.5 h deposited films, loosing pearls-chain like morphology (Figure 2e,f)). As a result, such a special pearls-chain morphology of the  $\text{Nb}_2\text{O}_5-\text{TiO}_2$  (1 h) electrode may enhance  $\text{Li}^+$  ions storage properties. Figure 2g shows the image of the cross-section of  $\text{Nb}_2\text{O}_5-\text{TiO}_2$  (1 h) electrode film. A layer of about 123.2 nm thick is measured between the platinum layer and the copper layer. However, a gold layer of about 5 nm thick (probably too thin to discern) is expected, since we gold-coated the specimen for conductivity before putting it in the FIB-SEM. Therefore, we assume that the rest of the 118 nm layer may be due to the  $\text{Nb}_2\text{O}_5-\text{TiO}_2$  materials. SEM images of Cu foil substrate,  $\text{Nb}_2\text{O}_5$  (1 h) and  $\text{TiO}_2$  (1 h) electrodes are presented in Figure S1.

The morphological and physical structure of the electrodes were further evaluated using AFM technique. Figure 3a-c

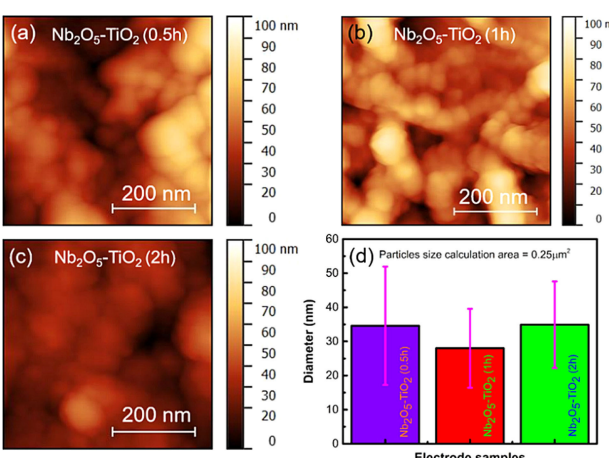


**Figure 3.** AFM topography images and average particle sizes of the electrodes: a-c) topography of a)  $\text{Nb}_2\text{O}_5-\text{TiO}_2$  (0.5 h). b)  $\text{Nb}_2\text{O}_5-\text{TiO}_2$  (1 h). c)  $\text{Nb}_2\text{O}_5-\text{TiO}_2$  (2 h) electrodes. d) average particle sizes measured within the area of  $0.25 \mu\text{m}^2$  from (a-c).

present AFM topography images with an area of  $0.25 \mu\text{m}^2$  ( $0.5 \mu\text{m} \times 0.5 \mu\text{m}$ ) obtained on the  $\text{Nb}_2\text{O}_5-\text{TiO}_2$  electrodes. Clearly, no significant difference is observed between  $\text{Nb}_2\text{O}_5-\text{TiO}_2$  (0.5 h) and  $\text{Nb}_2\text{O}_5-\text{TiO}_2$  (2 h) electrodes, however, pearls-chain like morphology is visualised in the image of  $\text{Nb}_2\text{O}_5-\text{TiO}_2$  (1 h) electrode. More AFM images of the electrodes can be found in Figure S2. An area of  $0.25 \mu\text{m}^2$  for each electrode was selected for the calculation of particles sizes as shown in Figure 3d. An approximate particle sizes were measured to be  $34 \pm 17$  nm for  $\text{Nb}_2\text{O}_5-\text{TiO}_2$  (0.5 h),  $28 \pm 11$  nm for  $\text{Nb}_2\text{O}_5-\text{TiO}_2$  (1 h), and  $35 \pm 12$  nm for  $\text{Nb}_2\text{O}_5-\text{TiO}_2$  (2 h) electrodes, respectively. Within the same area of  $0.25 \mu\text{m}^2$ , the measured average particle sizes were  $34 \pm 19$  nm for  $\text{Nb}_2\text{O}_5$  (1 h) and  $40 \pm 20$  nm for  $\text{TiO}_2$  (1 h) electrodes, respectively (Figure S3). AFM topography images and corresponding par-

ticles size analysis reveal that  $\text{Nb}_2\text{O}_5-\text{TiO}_2$  (1 h) electrode shows smaller particles size than that of the other electrodes.

To achieve more structural information of the electrodes, AFM data was used to evaluate the particles size distribution. Figure 4 a, c, e demonstrate AFM mages of the electrodes and

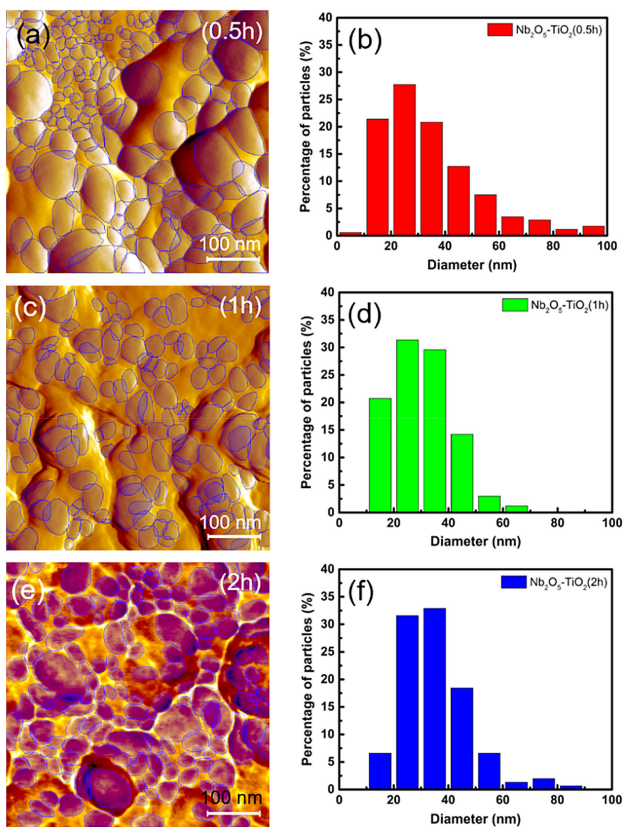


**Figure 4.** AFM images and corresponding particles size distribution: a, b)  $\text{Nb}_2\text{O}_5-\text{TiO}_2$  (0.5 h). c, d)  $\text{Nb}_2\text{O}_5-\text{TiO}_2$  (1 h). e, f)  $\text{Nb}_2\text{O}_5-\text{TiO}_2$  (2 h) electrodes.

their corresponding particles size distribution results are depicted in Figure 4b, d, f. As revealed in Figure 4b, d, f, particles size between 0–100 nm for  $\text{Nb}_2\text{O}_5-\text{TiO}_2$  (0.5 h), 10–70 nm for  $\text{Nb}_2\text{O}_5-\text{TiO}_2$  (1 h), and 10–90 nm for  $\text{Nb}_2\text{O}_5-\text{TiO}_2$  (2 h) electrodes are spotted. No particles size over 70 nm is realised in the  $\text{Nb}_2\text{O}_5-\text{TiO}_2$  (1 h) electrode. Overall, high percentage distribution of smaller particles is observed in the  $\text{Nb}_2\text{O}_5-\text{TiO}_2$  (1 h) electrode. We further conducted roughness evaluation of the electrodes in 3 different areas of  $900 \mu\text{m}^2$ ,  $1.0 \mu\text{m}^2$ , and  $0.25 \mu\text{m}^2$ , respectively. Figure 5a-c shows AFM topography within the area of  $900 \mu\text{m}^2$  ( $30 \mu\text{m} \times 30 \mu\text{m}$ ) and the measured corresponding surface area roughness is demonstrated in Figure 5d. Roughness of the  $\text{Nb}_2\text{O}_5-\text{TiO}_2$  (1 h) electrode film measured in 3 three different areas is higher than other two electrodes of  $\text{Nb}_2\text{O}_5-\text{TiO}_2$  (0.5 h) and  $\text{Nb}_2\text{O}_5-\text{TiO}_2$  (2 h) (Figure 5d, e, f), respectively, implying that higher surface area roughness of the  $\text{Nb}_2\text{O}_5-\text{TiO}_2$  (1 h) electrode may work as an electrolyte reservoir, which could facilitate electrolyte diffusion into the bulk of the electrode. AFM topography within the same area of  $900 \mu\text{m}^2$  ( $30 \mu\text{m} \times 30 \mu\text{m}$ ) and the measured

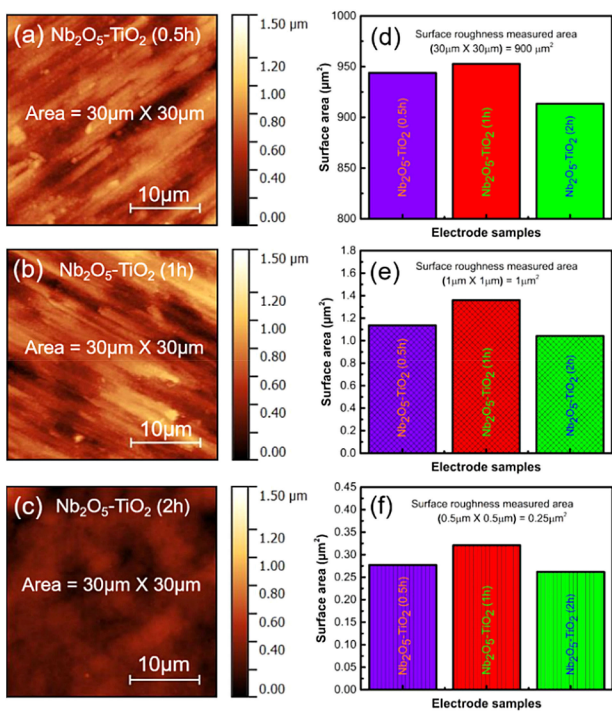


**Figure 5.** AFM topography and measured approximate values of surface area roughness parameter of the electrodes: a–c) AFM topography with area of  $900 \mu\text{m}^2$  ( $30 \mu\text{m} \times 30 \mu\text{m}$ ). d) corresponding surface area roughness values measured from (a–c) for the same area of  $900 \mu\text{m}^2$ . e, f) surface area roughness values measured from area of (e)  $1 \mu\text{m}^2$  ( $1 \mu\text{m} \times 1 \mu\text{m}$ ) and (f)  $0.25 \mu\text{m}^2$  ( $0.5 \mu\text{m} \times 0.5 \mu\text{m}$ ), respectively.

corresponding roughness for the  $\text{TiO}_2$  (1 h) and  $\text{Nb}_2\text{O}_5$  (1 h) electrodes can also be found in Figure S4.

To understand  $\text{Li}^+$  ions intercalation/de-intercalation behaviour of the electrode films, cyclic voltammetry (CV) was carried out within the potential range of 1.0–3.0 V (vs Li/Li<sup>+</sup>) at a scan rate of  $0.5 \text{ mVs}^{-1}$ . Figure 6 compares the CV curves between  $\text{Nb}_2\text{O}_5$ ,  $\text{TiO}_2$ , and  $\text{Nb}_2\text{O}_5-\text{TiO}_2$  electrodes. Electrodes fabricated with 1.0 h deposition time were selected for CV analysis. As shown in Figure 6a for  $\text{Nb}_2\text{O}_5$  electrode, cathodic peaks at  $\sim 1.3 \text{ V}$  in the 1<sup>st</sup> cycle and  $\sim 1.4 \text{ V}$  in the subsequent cycles (reduction- $\text{Nb}^{5+}/\text{Nb}^{4+}$ ) and anodic peaks at  $\sim 2.0 \text{ V}$  (oxidation- $\text{Nb}^{4+}/\text{Nb}^{5+}$ ) were detected.<sup>[16]</sup> A redox peaks of 1.4/2.0 V represents intercalation/de-intercalation process of  $\text{Li}^+$  ions into the crystal structure of the  $\text{Nb}_2\text{O}_5$  electrode according to the equation below:

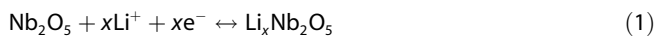
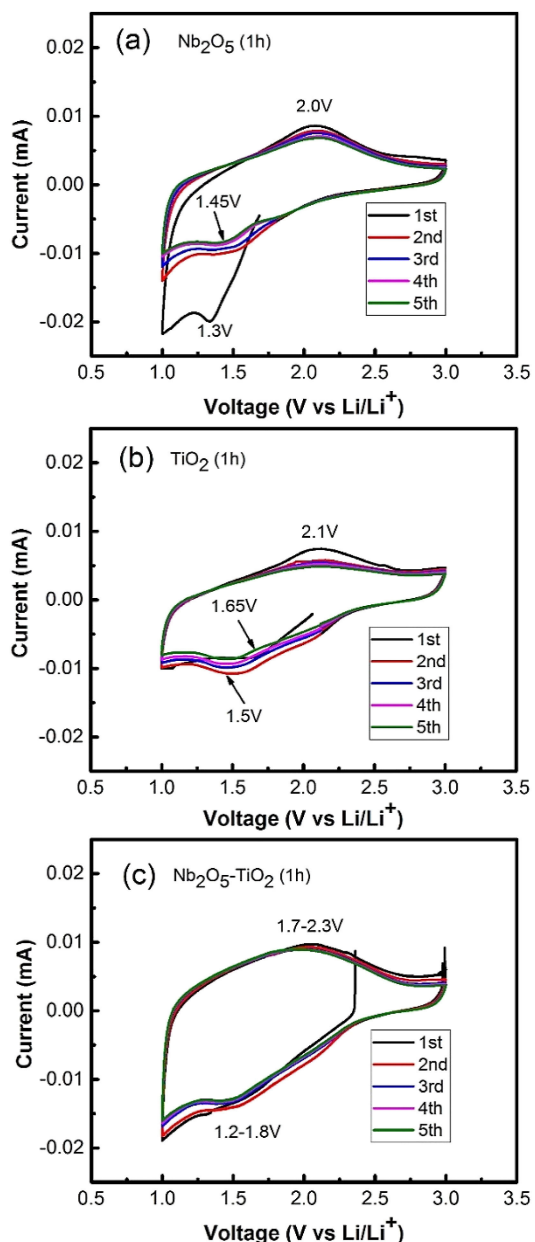


Figure 6b shows the representative CV curves of the rutile  $\text{TiO}_2$ . In the cathodic scan, peaks at  $\sim 1.6 \text{ V}$  in the 1<sup>st</sup> cycle and  $\sim 1.5 \text{ V}$  in the subsequent cycles was observed. A redox peaks (cathodic/anodic) at  $\sim 1.5/2.1 \text{ V}$  was maintained in the subsequent cycles.<sup>[45,46]</sup> The intercalation/de-intercalation process of  $\text{Li}^+$  ions into the crystal structure of the rutile  $\text{TiO}_2$  can be summarised as below:



**Figure 6.** Cyclic voltammograms of the Nb<sub>2</sub>O<sub>5</sub> (1 h), TiO<sub>2</sub> (1 h) and Nb<sub>2</sub>O<sub>5</sub>-TiO<sub>2</sub> (1 h) electrodes at a scan rate 0.5 mVs<sup>-1</sup> within the potential range of 1.0–3.0 V (vs Li/Li<sup>+</sup>).



In the case of hybridized Nb<sub>2</sub>O<sub>5</sub>-TiO<sub>2</sub> electrode, however, broad cathodic and anodic peaks are formed (Figure 6c), which could be related to the combination of Nb<sub>2</sub>O<sub>5</sub> peak and TiO<sub>2</sub> peak together. A broad cathodic peak located in the range of 1.2–1.8 V, corresponds to the potential profiles of the discharge process, involving Li<sup>+</sup> ions intercalation first in to the crystal structure of TiO<sub>2</sub> followed by Nb<sub>2</sub>O<sub>5</sub> in the Nb<sub>2</sub>O<sub>5</sub>-TiO<sub>2</sub> electrode. Similarly, broad anodic peak located at ~1.7–2.3 V is corresponding to the charge process, involving Li<sup>+</sup> ions de-intercalation from the crystal structure of the Nb<sub>2</sub>O<sub>5</sub>-TiO<sub>2</sub> electrode. The CV curve of the first and fifth cycles almost

overlap, demonstrating good reversibility of the electrochemical reactions in the Nb<sub>2</sub>O<sub>5</sub>-TiO<sub>2</sub> electrode after the initial cycle.

Figure 7a compares electrochemical performance between Nb<sub>2</sub>O<sub>5</sub>-TiO<sub>2</sub> (0.5 h), Nb<sub>2</sub>O<sub>5</sub>-TiO<sub>2</sub> (1 h), and Nb<sub>2</sub>O<sub>5</sub>-TiO<sub>2</sub> (2 h) electrodes, respectively. The Nb<sub>2</sub>O<sub>5</sub>-TiO<sub>2</sub> (1 h) electrode displays a high reversible capacity of 214 mAh g<sup>-1</sup> at 50 mA g<sup>-1</sup>; areal 0.0214 mAh cm<sup>-2</sup> at 5 μA cm<sup>-2</sup> and volumetric 1,813 mAh cm<sup>-3</sup> at 5 μA cm<sup>-2</sup> after 500 cycles. Relatively low reversible capacities of 105 mAh g<sup>-1</sup> for Nb<sub>2</sub>O<sub>5</sub>-TiO<sub>2</sub> (0.5 h) and 163 mAh g<sup>-1</sup> for Nb<sub>2</sub>O<sub>5</sub>-TiO<sub>2</sub> (2 h) electrodes were measured in an identical testing condition. Galvanostatic charge-discharge profiles of the Nb<sub>2</sub>O<sub>5</sub>-TiO<sub>2</sub> (1 h) electrode are demonstrated in Figure 7b. Figure 7b shows the 1<sup>st</sup> and 2<sup>nd</sup> cycles charge-discharge potential profiles and profile for other selected cycles of 100, 200, 300, 400, and 500<sup>th</sup>, respectively. It is important to note that Nb<sub>2</sub>O<sub>5</sub>-TiO<sub>2</sub> (1 h) electrode displays sloping charge-discharge profiles rather than obvious plateau (results are quite consistence with the CV curves), which could be related to the low crystallinity of the sample.<sup>[47,48]</sup> A large capacity of 510 mAh g<sup>-1</sup> was measured in the first discharge process whereas charge capacity was 372 mAh g<sup>-1</sup>, even though delivering a commendable Coulombic efficiency of ~73% in the first cycle, however, this irreversible capacity loss could be related to the side reactions of the electrode materials.<sup>[47]</sup> High Coulombic efficiency of ~100% was achieved for all electrodes after initial few cycles, indicating very good reversibility of the electrodes (Figure 7a).

The influence of deposition time on the electrochemical performance was further investigated by rate capability test of the electrodes (Figure 7c). The obtained data show that the Nb<sub>2</sub>O<sub>5</sub>-TiO<sub>2</sub> (1 h) electrode exhibits superior rate performance over Nb<sub>2</sub>O<sub>5</sub>-TiO<sub>2</sub> (0.5 h) and Nb<sub>2</sub>O<sub>5</sub>-TiO<sub>2</sub> (2 h) electrodes. The reversible capacities of 261 mAh g<sup>-1</sup> at 0.1 A g<sup>-1</sup>; 211 mAh g<sup>-1</sup> at 0.2 A g<sup>-1</sup>; 176 mAh g<sup>-1</sup> at 0.3 A g<sup>-1</sup>; 159 mAh g<sup>-1</sup> at 0.6 A g<sup>-1</sup>; 137 mAh g<sup>-1</sup> at 1.5 A g<sup>-1</sup>; 126 mAh g<sup>-1</sup> at 3.0 A g<sup>-1</sup>; and 115 mAh g<sup>-1</sup> at 6.0 A g<sup>-1</sup> were achieved for the Nb<sub>2</sub>O<sub>5</sub>-TiO<sub>2</sub> (1 h) electrode. A capacity recovery of 231 mAh g<sup>-1</sup> (88.5% retention) was obtained when electrode was brought back to 0.1 A g<sup>-1</sup> after 50 cycles whereas it was 133 mAh g<sup>-1</sup> (82% retention) for Nb<sub>2</sub>O<sub>5</sub>-TiO<sub>2</sub> (0.5 h) and 182 mAh g<sup>-1</sup> (80% retention) for Nb<sub>2</sub>O<sub>5</sub>-TiO<sub>2</sub> (2 h) electrodes, respectively. Such an excellent electrochemical performance of the Nb<sub>2</sub>O<sub>5</sub>-TiO<sub>2</sub> (1 h) electrode was further investigated as shown in Figure 7d. The electrode is capable to sustain over long-term 1000 cycles with a retained capacity of gravimetric 174 mAh g<sup>-1</sup> at 0.4 A g<sup>-1</sup>; areal 0.0174 mAh cm<sup>-2</sup> at 40 μA cm<sup>-2</sup> and volumetric 1,474 mAh cm<sup>-3</sup> at 40 μA cm<sup>-2</sup>. A high Coulombic efficiency of almost 100% was maintained over 1000 cycles (Figure 7d).

As the Nb<sub>2</sub>O<sub>5</sub>-TiO<sub>2</sub> (1 h) electrode exhibits better electrochemical performance over Nb<sub>2</sub>O<sub>5</sub>-TiO<sub>2</sub> (0.5 h) and Nb<sub>2</sub>O<sub>5</sub>-TiO<sub>2</sub> (2 h) electrodes, therefore, Nb<sub>2</sub>O<sub>5</sub>-TiO<sub>2</sub> (1 h) electrode was compared to the single-phase electrode of only Nb<sub>2</sub>O<sub>5</sub> or TiO<sub>2</sub>. For this comparison, Nb<sub>2</sub>O<sub>5</sub> and TiO<sub>2</sub> electrode films were fabricated using the same conditions as it does for the Nb<sub>2</sub>O<sub>5</sub>-TiO<sub>2</sub> (1 h) electrode. Figure 8a reveals electrochemical performance between electrodes and shows that Nb<sub>2</sub>O<sub>5</sub>-TiO<sub>2</sub> (1 h) is capable to achieve a discharge capacity of 218 mAh g<sup>-1</sup>

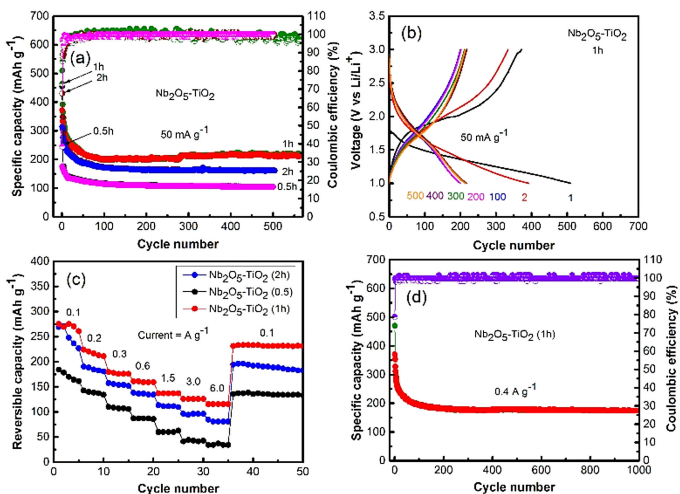


**Figure 7.** Electrochemical performance of the electrodes: a) cycling performance and corresponding Coulombic efficiencies of the electrodes at a current density of  $50 \text{ mA g}^{-1}$ . b) corresponding charge-discharge potential profiles obtained at  $50 \text{ mA g}^{-1}$  for the selected cycles of the  $\text{Nb}_2\text{O}_5\text{-TiO}_2$  (1 h) electrode. c) rate capability test at different current densities. d) long-term cycling performance and corresponding Coulombic efficiency of the  $\text{Nb}_2\text{O}_5\text{-TiO}_2$  (1 h) electrode at a current density of  $0.4 \text{ A g}^{-1}$  up to 1000 cycles.

at  $50 \text{ mA g}^{-1}$  after 400 cycles, which is better than that of  $177 \text{ mAh g}^{-1}$  for  $\text{TiO}_2$  (1 h) and  $155 \text{ mAh g}^{-1}$  for  $\text{Nb}_2\text{O}_5$  (1 h) electrodes, respectively. The capacity retention of  $\sim 43\%$  (in respect to initial discharge capacity) is also measured for  $\text{Nb}_2\text{O}_5\text{-TiO}_2$  (1 h) electrode, higher than  $\text{Nb}_2\text{O}_5$  (1 h) (30%) and  $\text{TiO}_2$  (1 h) (34%). Figure 8a also compares Coulombic efficiencies between electrodes. The initial Coulombic efficiencies of  $\sim 73$ , 67, and 55% were measured for the  $\text{Nb}_2\text{O}_5\text{-TiO}_2$  (1 h),  $\text{TiO}_2$  (1 h), and  $\text{Nb}_2\text{O}_5$  (1 h) electrodes, respectively. Galvanostatic charge-discharge profiles of the  $\text{Nb}_2\text{O}_5$  (1 h) and  $\text{TiO}_2$  (1 h) electrodes obtained at  $50 \text{ mA g}^{-1}$  for the selected cycles of 1<sup>st</sup>, 2<sup>nd</sup>, 100<sup>th</sup>, 200<sup>th</sup>, 300<sup>th</sup>, and 400<sup>th</sup> are shown in Figure 8b, c. However, capacities of all electrodes decrease sharply for the initial several cycles and stabilise in the extended cycling. During initial intercalation,  $\text{Li}^+$  ions are inserted into the  $\text{Nb}_2\text{O}_5\text{-TiO}_2$  or  $\text{Nb}_2\text{O}_5$  or  $\text{TiO}_2$  electrode thin films. Some of these  $\text{Li}^+$  ions are trapped and cannot fully reverse in the charge process because some of the extra sites in the electrodes are irreversible for  $\text{Li}^+$  ions.<sup>[49]</sup> It is anticipated that more and more inactive  $\text{Li}^+$  ions are accumulated in the electrode material. This process naturally intensifies the rate of electrolyte decomposition and the subsequent SEI formation for the initial several cycles.<sup>[50,51]</sup> This phenomenon may account for the observed capacity loss in the initial several cycles.

An inspiring electrochemical performance of the hybrid  $\text{Nb}_2\text{O}_5\text{-TiO}_2$  electrode is not only better than single-phase electrode of either  $\text{Nb}_2\text{O}_5$  or  $\text{TiO}_2$ , but also even better than other reported additive-based  $\text{Nb}_2\text{O}_5$  and  $\text{TiO}_2$  systems, as summarized in Table S1.<sup>[12,16,19,38,52–58]</sup> The superior electrochemical performance of the  $\text{Nb}_2\text{O}_5\text{-TiO}_2$  (1 h) electrode over  $\text{Nb}_2\text{O}_5\text{-TiO}_2$  (0.5 h),  $\text{Nb}_2\text{O}_5\text{-TiO}_2$  (2 h),  $\text{Nb}_2\text{O}_5$  (1 h) and  $\text{TiO}_2$  (1 h) electrodes can be credited to its distinctive electrode architecture and synergistic effects between component as described below:

First, SEM and AFM observations demonstrate that  $\text{Nb}_2\text{O}_5\text{-TiO}_2$  (1 h) electrode film features pearls-chain like morphology consisting of numerous nanoparticles, which are attached one after one. Such a unique arrangement is capable to form void due to the interconnection gaps among chains. Once impregnated by the electrolyte, the voids function as an electrolyte reservoir, facilitates electrolyte diffusion into the bulk of the electrode, thus improving  $\text{Li}^+$  ions transport path.

Second, among all electrode films, the  $\text{Nb}_2\text{O}_5\text{-TiO}_2$  (1 h) electrode shows small particles size ( $28 \pm 11 \text{ nm}$ ). Smaller particles not only improve ionic conductivity but also minimise extra strain developing in the electrode during repeated cycling process. Hence,  $\text{Nb}_2\text{O}_5\text{-TiO}_2$  (1 h) electrode is accomplished to bear repeated expansion and contraction much better than other electrodes by enabling charge transfer (both ionic and electronic) over shorter distances.

Third, roughness of the electrode films is another important factor needs to be considered. Higher roughness is measured for the  $\text{Nb}_2\text{O}_5\text{-TiO}_2$  (1 h) electrode film as shown in Figure 5. High surface roughness could hold electrolyte and provide large effective area for most particles contribution to the charge-discharge process. Additionally, during cycling both  $\text{Nb}_2\text{O}_5$  and  $\text{TiO}_2$  nanoparticles act as mutual buffer due to synergistic effect which has an encouraging impact in controlling the volume change effects in the electrode,<sup>[12,41]</sup> promoting a better electrochemical performance of the  $\text{Nb}_2\text{O}_5\text{-TiO}_2$  electrode over their counter part of  $\text{Nb}_2\text{O}_5$  or  $\text{TiO}_2$ .

Fourth, as binder is not used in the  $\text{Nb}_2\text{O}_5\text{-TiO}_2$  (1 h) electrode system, therefore grain boundaries and interface charge transfer resistance are likely to be reduced significantly.<sup>[59]</sup> As a result, high electron transport along the lattices of electroactive  $\text{Nb}_2\text{O}_5\text{-TiO}_2$  is expected. Furthermore, a tight contact between  $\text{Nb}_2\text{O}_5\text{-TiO}_2$  and the surface of conductive Cu foil substrate is also realised which permits for rapid electron

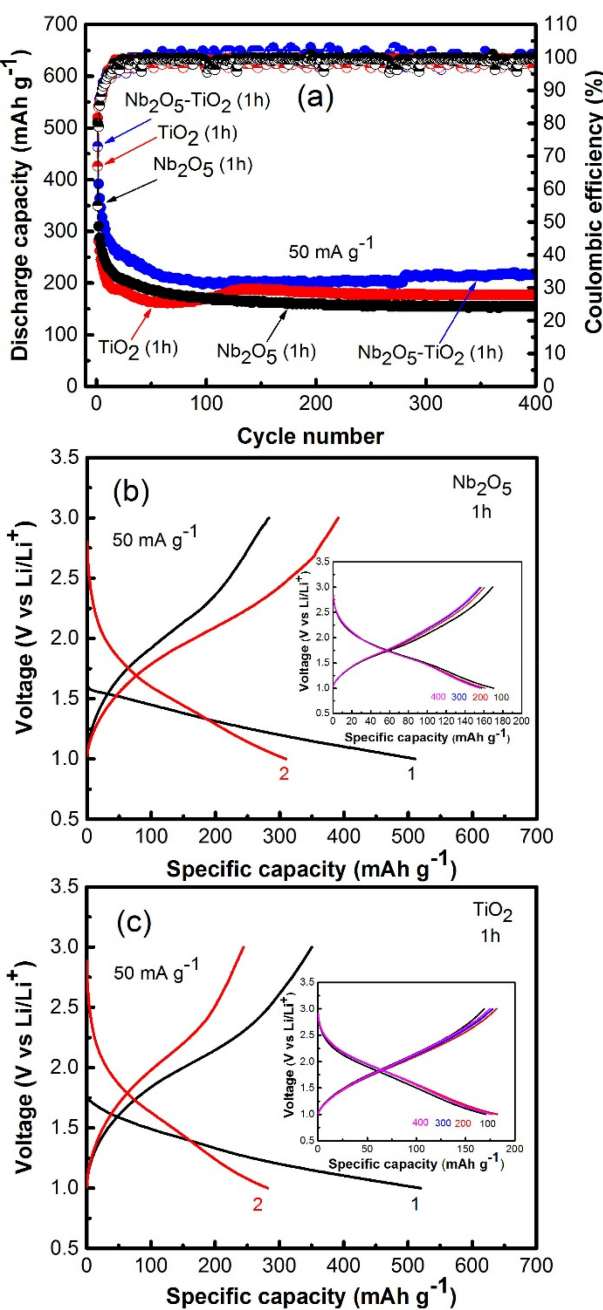


**Figure 8.** Electrochemical performance of the Nb<sub>2</sub>O<sub>5</sub>-TiO<sub>2</sub> (1 h), Nb<sub>2</sub>O<sub>5</sub> (1 h), and TiO<sub>2</sub> (1 h) electrodes: a) cycling performance and corresponding Coulombic efficiencies at a current density of 50 mA g<sup>-1</sup> up to 400 cycles. b,c) corresponding charge-discharge profiles obtained at 50 mA g<sup>-1</sup> for the selected cycles (inset shows the curves for the 100<sup>th</sup>, 200<sup>th</sup>, 300<sup>th</sup>, and 400<sup>th</sup> cycle) of the Nb<sub>2</sub>O<sub>5</sub> (1 h) and TiO<sub>2</sub> (1 h) electrodes, respectively.

collection and transportation to the outer circuit, providing high rate capability of the cell.

### 3. Conclusions

In summary, we have developed one-step sputtering technique to achieve an additive-free hybrid electrode of Nb<sub>2</sub>O<sub>5</sub>-TiO<sub>2</sub> by

combining titanium (Ti) and niobium (Nb) target together. The process is fast, easy, and environment friendly which requires no additional chemicals/reagents. The electrode was used directly after being deposited on the copper (Cu) foil. The hybrid Nb<sub>2</sub>O<sub>5</sub>-TiO<sub>2</sub> electrode with 1 h deposition time demonstrates superior electrochemical performance over single-phase electrode of either Nb<sub>2</sub>O<sub>5</sub> or TiO<sub>2</sub> film. Furthermore, the hybrid Nb<sub>2</sub>O<sub>5</sub>-TiO<sub>2</sub> electrode is also dominating electrochemical performance over other reported additive-based Nb<sub>2</sub>O<sub>5</sub>-TiO<sub>2</sub> or Nb<sub>2</sub>O<sub>5</sub> or TiO<sub>2</sub> systems. The superior electrochemical performance of the Nb<sub>2</sub>O<sub>5</sub>-TiO<sub>2</sub> electrode could be accredited to its pearls-chain like architecture, small particles size, high surface roughness, and synergistic coupling effects from individual component. Our electrode fabrication strategy can potentially be used to fabricate a wide range of additive free electrodes (anode and cathode) for advanced energy storage technologies.

## Experimental Section

### Fabrication of Nb<sub>2</sub>O<sub>5</sub>-TiO<sub>2</sub> Electrode Films

The ONYX-2™ Magnetron Sputtering was used for the fabrication of Nb<sub>2</sub>O<sub>5</sub>-TiO<sub>2</sub> electrode films. During deposition, both Ti and Nb targets were used together where copper (Cu) foil used as substrate. The Cu foil substrate was placed on the sample holder and then the holder was inserted inside the chamber. The process was carried out under vacuum with a sputtering gas flow, a mixture of pure argon/oxygen (Ar/O<sub>2</sub>) of 30/15 sccm. A radio frequency power of 250 W was applied to the targets. Three different deposition times of 0.5, 1.0, and 2.0 h was selected. For comparison, an identical condition was used to fabricate Nb<sub>2</sub>O<sub>5</sub> and TiO<sub>2</sub> electrode film using only Nb and Ti target, respectively. According to the deposition time, the fabricated electrodes were identified as Nb<sub>2</sub>O<sub>5</sub>-TiO<sub>2</sub> (0.5 h), Nb<sub>2</sub>O<sub>5</sub>-TiO<sub>2</sub> (1 h), Nb<sub>2</sub>O<sub>5</sub>-TiO<sub>2</sub> (2 h), Nb<sub>2</sub>O<sub>5</sub> (1 h), and TiO<sub>2</sub> (1 h), respectively.

### Films Characterization

X-ray diffraction (XRD) data were collected from the film samples on a PANalytical X'Pert Pro instrument using a CuK $\alpha$  radiation source ( $\lambda = 1.54181 \text{ \AA}$ ) and operated at 40 kV with a 50 mA current. A Kratos AXIS Nova spectrometer (Kratos Analytical Ltd, U.K.) equipped with a monochromated Al K  $\alpha$  X-ray source ( $h\nu = 1486.6 \text{ eV}$ ) operating at 150 W used for X-ray photoelectron spectroscopy (XPS) analysis. Morphologies of all film samples were examined using scanning electron microscopy (SEM, Carl Zeiss Supra 55 VP Instrument). Thicknesses of the electrode was measured by FEI Quanta 3D FEG (SEM/FIB) microscope using the Everhart-Thornley detector. An atomic force microscope (AFM, Cypher Asylum Research) was used to analyse topography, particles size and particles size distribution of the electrode films.

### Electrochemical Characterization

Thin film electrodes of Nb<sub>2</sub>O<sub>5</sub>-TiO<sub>2</sub>, Nb<sub>2</sub>O<sub>5</sub>, and TiO<sub>2</sub> were used directly for the assembly of CR-2032 coin-type cells where Li foil as the counter/reference electrode and a microporous polypropylene film used as a separator. An electrolyte of 1 M LiPF<sub>6</sub> in a mixture of ethylene carbonate (EC) and diethylene carbonate (DEC) with a volume ratio of 1:1 was used. Galvanostatic discharge-charge on

the cells was performed within the cut-off voltages of 1.0–3.0 V (vs Li/Li<sup>+</sup>) at different current densities using a Land Battery Testing System.

## Acknowledgements

The work was supported by ARC Discovery Project [DP110101188], National Key R&D Program of China (2016YFA0200200), DICP & QIBEBT (Grant DICP & QIBEBT UN201702), Dalian National Laboratory For Clean Energy (DNL), CAS. Authors also acknowledge the use of Deakin Advanced Characterization Facilities. All authors discussed the results and contributed equally.

## Conflict of Interest

The authors declare no conflict of interest.

**Keywords:** additive-free electrodes • battery safety • hybrid Nb<sub>2</sub>O<sub>5</sub>–TiO<sub>2</sub> anodes • lithium-ion batteries • sputtering

- [1] Y. Tang, Y. Zhang, W. Li, B. Ma, X. Chen, *Chem. Soc. Rev.* **2015**, *44*, 5926.  
[2] V. Etacheri, R. Marom, R. Elazari, G. Salitra, D. Aurbach, *Energy Environ. Sci.* **2011**, *4*, 3243.  
[3] G. E. Blomgren, *J. Electrochem. Soc.* **2017**, *164*, A5019.  
[4] Z. Chen, I. Belharouak, Y. K. Sun, K. Amine, *Adv. Funct. Mater.* **2013**, *23*, 959.  
[5] H. Ren, R. B. Yu, J. Y. Wang, Q. Jin, M. Yang, D. Mao, D. Kisailus, H. J. Zhao, D. Wang, *Nano Lett.* **2014**, *14*, 6679.  
[6] Y. Luo, J. Luo, J. Jiang, W. Zhou, H. Yang, X. Qi, H. Zhang, H. J. Fan, D. Y. W. Yu, C. M. Li, T. Yu, *Energy Environ. Sci.* **2012**, *5*, 6559.  
[7] Z. Wang, L. Zhou, X. W. Lou, *Adv. Mater.* **2012**, *24*, 1903.  
[8] Z. Yang, D. Choi, S. Kerisit, K. M. Rosso, D. Wang, J. Zhang, G. Graff, J. Liu, *J. Power Sources* **2009**, *192*, 588.  
[9] Y. Zhang, Y. Tang, W. Li, X. Chen, *ChemNanoMat* **2016**, *2*, 764.  
[10] E. Baudrin, S. Cassaignon, M. Koelsch, J. P. Jolivet, L. Dupont, J. M. Tarascon, *Electrochem. Commun.* **2007**, *9*, 337.  
[11] P. Kubiak, M. Pfanzelta, J. Geserick, U. Hörmann, N. Hüsing, U. Kaiser, M. Wohlfahrt-Mehrens, *J. Power Sources* **2009**, *194*, 1099.  
[12] Y. Liu, L. Lin, W. Zhang, M. Wei, *Sci. Rep.* **2017**, *7*, 7204.  
[13] V. Augustyn, J. Come, M. A. Lowe, J. W. Kim, P. L. Taberna, S. H. Tolbert, H. D. Abruña, P. Simon, B. Dunn, *Nat. Mater.* **2013**, *12*, 518.  
[14] J. Come, V. Augustyn, J. W. Kim, P. Rozier, P. L. Taberna, P. Gogotsi, J. W. Long, B. Dunn, P. Simon, *J. Electrochem. Soc.* **2014**, *161*, A718.  
[15] J. W. Kim, V. Augustyn, B. Dunn, *Adv. Energy Mater.* **2012**, *2*, 141.  
[16] M. M. Rahman, R. A. Rani, A. Z. Sadek, A. S. Zoofkar, M. R. Field, T. Ramireddy, K. K. Zadeh, Y. Chen, *J. Mater. Chem. A* **2013**, *1*, 11019.  
[17] K. Brezesinski, J. Wang, J. Haetge, C. Reitz, S. O. Steinmueller, S. H. Tolbert, B. M. Smarsly, B. Dunn, T. Brezesinski, *J. Am. Chem. Soc.* **2010**, *132*, 6982.  
[18] X. Wang, G. Li, Z. Chen, V. Augustyn, X. Ma, G. Wang, B. Dunn, Y. Lu, *Adv. Energy Mater.* **2011**, *1*, 1089.  
[19] G. Li, X. Wang, X. Ma, *J. Energy Chem.* **2013**, *22*, 357.  
[20] M. Wei, K. Wei, M. Ichihara, H. Zhou, *Electrochem. Commun.* **2008**, *10*, 980.  
[21] H. Shim, Y. H. Jin, S. D. Seo, S. H. Lee, D. W. Kim, *ACS Nano* **2011**, *5*, 443.  
[22] P. G. Bruce, B. Scrosati, J. M. Tarascon, *Angew. Chem. Int. Ed.* **2008**, *47*, 2930.  
[23] Y. G. Wang, H. Q. Li, P. He, E. Hosono, H. S. Zhou, *Nanoscale* **2010**, *2*, 1294.  
[24] Z. Chen, V. Augustyn, J. Wen, Y. W. Zhang, M. Q. Shen, B. Dunn, Y. F. Lu, *Adv. Mater.* **2011**, *23*, 791.  
[25] I. Kovalenko, D. G. Bucknall, G. Yushin, *Adv. Funct. Mater.* **2010**, *20*, 3979.  
[26] M. H. Park, K. Kim, J. Kim, J. Cho, *Adv. Mater.* **2010**, *22*, 415.  
[27] J. Gao, M. A. Lowe, H. C. D. Abruna, *Chem. Mater.* **2011**, *23*, 3223.  
[28] Z. S. Wu, W. Ren, L. Wen, L. Gao, J. Zhao, Z. Chen, G. Zhou, F. Li, H. M. Cheng, *ACS Nano* **2010**, *4*, 3187.  
[29] H. Wang, L. F. Cui, Y. Yang, C. H. Sanchez, J. T. Robinson, Y. Liang, Y. Cui, H. Dai, *J. Am. Chem. Soc.* **2010**, *132*, 13978.  
[30] L. Sun, W. Liu, Y. Cui, Y. Zhang, H. Wang, S. Liu, B. Shan, *Green Chem.* **2018**, DOI: 10.1039/c8gc01683f.  
[31] D. H. Ha, M. A. Islam, R. D. Robinson, *Nano Lett.* **2012**, *12*, 5122.  
[32] S. Grueon, S. Larruelle, R. Herrera-Urbina, L. Dupont, P. Poizot, J. M. Tarascon, *J. Electrochem. Soc.* **2001**, *148*, A285.  
[33] C. K. Chan, H. L. Peng, G. Liu, K. McIlwrath, X. F. Zhang, R. A. Huggins, Y. Cui, *Nat. Nanotechnol.* **2008**, *3*, 31.  
[34] A. M. Chockla, J. T. Harris, V. A. Akhavan, T. D. Bogart, V. C. Holmberg, C. Steinhagen, C. B. Mullins, K. J. Stevenson, B. A. Korgel, *J. Am. Chem. Soc.* **2011**, *133*, 20914.  
[35] Y. Li, X. Lv, J. Li, *Appl. Phys. Lett.* **2009**, *95*, 113102.  
[36] C. C. Li, Q. H. Li, L. B. Chen, T. H. Wang, *J. Mater. Chem.* **2011**, *21*, 11867.  
[37] H. Wu, G. Chan, J. W. Choi, I. Ryu, Y. Yao, M. T. McDowell, S. W. Lee, A. Jackson, Y. Yang, L. Hu, Y. Cui, *Nat. Nanotechnol.* **2012**, *7*, 310.  
[38] X. Yu, L. Xin, Y. Liu, W. Zhao, B. Li, X. Zhou, H. Shena, *RSC Adv.* **2016**, *6*, 27094.  
[39] W. Shi, X. Rui, J. Zhu, Q. Yan, *J. Phys. Chem. C* **2012**, *116*, 26685.  
[40] M. Srivastava, J. Singh, T. Kuila, R. K. Layek, N. H. Kime, J. H. Lee, *Nanoscale* **2015**, *7*, 4820.  
[41] J. Wang, Q. Deng, M. Li, K. Jiang, J. Zhang, Z. Hu, J. Chu, *Sci. Rep.* **2017**, *7*, 8903.  
[42] S. Ge, H. Jia, H. Zhao, Z. Zheng, L. Zhang, *J. Mater. Chem.* **2010**, *20*, 3052.  
[43] Y. Y. Zhao, S. P. Pang, C. J. Zhang, Q. X. Zhang, L. Gu, X. H. Zhou, G. C. Li, G. L. Cui, *J. Solid State Electrochem.* **2013**, *17*, 1479.  
[44] Z. N. Wan, R. Cai, S. M. Jiang, Z. P. Shao, *J. Mater. Chem.* **2012**, *22*, 17773.  
[45] J. S. Chen, X. W. Lou, *J. Power Sources* **2010**, *195*, 2905.  
[46] X. Y. Yu, H. B. Wu, L. Yu, F. X. Ma, X. W. (David) Lou, *Angew. Chem. Int. Ed.* **2015**, *54*, 4001.  
[47] J. Li, Z. Tang, Z. Zhang, *Electrochem. Commun.* **2005**, *7*, 894.  
[48] M. M. Rahman, J. Z. Wang, D. Wexler, Y. Y. Zhang, X. J. Li, S. L. Chou, H. K. Liu, *J. Power Sources* **2010**, *195*, 4297.  
[49] J. Wang, Y. Zhou, Y. Hu, R. O'Hare, Z. Shao, *J. Phys. Chem. C* **2011**, *115*, 2529.  
[50] J. Li, Z. Tang, Z. Zhang, *Electrochem. Solid-State Lett.* **2005**, *8*, A316.  
[51] M. M. Rahman, J. Z. Wang, D. Wexler, Y. Y. Zhang, X. J. Li, S. L. Chou, H. K. Liu, *J. Solid State Electrochem.* **2010**, *14*, 571.  
[52] G. Kim, C. Jo, W. Kim, J. Chun, S. Yoon, J. Lee, W. Choi, *Energy Environ. Sci.* **2013**, *6*, 2932.  
[53] M. Liu, C. Yan, Y. Zhang, *Sci. Rep.* **2015**, *5*, 8326.  
[54] S. Liu, J. Zhou, Z. Cai, G. Fang, A. Pan, S. Liang, *Nanotechnology* **2016**, *27*, 46LT01.  
[55] M. Sasidharan, N. Gunawardhana, M. Yoshio, K. Nakashima, *Mater. Res. Bull.* **2012**, *47*, 2161.  
[56] T. Lan, H. Qiu, F. Xie, J. Yang, M. Wei, *Sci. Rep.* **2015**, *5*, 8498.  
[57] M. Zhen, X. Guo, G. Gao, Z. Zhou, L. Liu, *Chem. Commun.* **2014**, *50*, 11915.  
[58] D. McNulty, E. Carroll, C. O'Dwyer, *Adv. Energy Mater.* **2017**, *7*, 1602291.  
[59] F. Zhang, L. Qi, *Adv. Sci.* **2016**, *3*, 1600049.

Manuscript received: September 13, 2018

Revised manuscript received: October 29, 2018

Version of record online: November 20, 2018